RSC Advances

PAPER

View Article Online
View Journal | View Issue

Cite this: *RSC Adv.*, 2020, **10**, 41127

Mechanism for hydrogen evolution from water splitting based on a MoS_2/WSe_2 heterojunction photocatalyst: a first-principle study

Yazhou Wang,[ab] Tong Liu,[ab] Weizhi Tian,[ab] Ying Zhang,[ab] Pengyue Shan,[ab] Yunjian Chen,[ab] Wanhang Wei,[ab] Hongkuan Yuan[c] and Hong Cui*[ab]

Received 12th August 2020
Accepted 5th November 2020

DOI: 10.1039/d0ra06939f

rsc.li/rsc-advances

In this study, density functional theory and hybrid functional theory are used to calculate the work function and energy band structure of MoS_2 and WSe_2, as well as the binding energy, work function, energy band structure, density of states, charge density difference, energy band alignment, Bader charge, and H adsorption free energy of MoS_2/WSe_2. The difference in work function led to the formation of a built-in electric field from WSe_2 to MoS_2, and the energy band alignment indicated that the redox reactions were located on the MoS_2 and WSe_2 semiconductors, respectively. The binding energy of MoS_2 and WSe_2 indicated that the thermodynamic properties of the heterogeneous structure were stable. MoS_2 and WSe_2 gathered electrons and holes, respectively, and redistributed them under the action of the built-in electric field. The photogenerated electrons and holes were enriched on the surface of WSe_2 and MoS_2, which greatly improved the efficiency of hydrogen production by photocatalytic water splitting.

Introduction

To further develop high-energy green hydrogen, the production of hydrogen using photocatalytic water splitting (WS) has attracted significant interest from both academia and industry.[1] During light irradiation, electrons in photocatalyst valence bands (VB) absorb photon energy and then become excited from the VB to the conduction bands (CB). This enables them to participate in the hydrogen evolution reaction (HER). The holes left in the VB can then participate in the oxygen evolution reaction (OER). This is another reaction for WS that is more difficult than the HER.[2,3]

After Fujishima and Honda used the photocatalyst TiO_2 for WS to successfully produce hydrogen in 1972,[4] researchers became committed to developing better photocatalysts for producing hydrogen.[5] Photocatalytic hydrogen generation by WS must meet two photocatalyst requirements under light conditions. The first requirement is that the energy to excite electrons from the VB of the photocatalytic to their CB must be greater than the WS voltage and the semiconductor bandgap. The second requirement is the CB potential in the energy band needs to be more negative than the hydrogen reduction potential, and the VB potential must be more positive than the oxidation potential.[5–7] According to the equation $\lambda = 1240/E_g$ (λ (nm), E_g represent the optical wavelength and semiconductor band gap), appropriately reducing the semiconductor band gap in excess of that required for WS (theoretically 1.23 eV) can reduce the requirements for the energy that the electron absorbs from light, broaden the light absorption range, and improve the efficiency of hydrogen evolution.[8]

Since the method of exfoliating graphene was discovered,[9] two-dimensional (2D) materials research has been developing rapidly, including transition metal dichalcogenides (TMD), especially for the monolayer TMD,[10] which has excellent optoelectronic properties compared with bulk TMD, such as superconductivity and a semiconducting behavior.[11,12] According to Voiry's research, TMDs, when used as photocatalysts, can broaden the range ($\geq$420 nm) of light absorption of visible light, but its stability and activity is not satisfactory.[13] The atomic-thickness monolayer MoS_2, which features good low light detection,[14] high photosensitivity, and high carrier mobility, has high light absorption efficiency and generates a large number of photogenerated electrons and hole pairs under light conditions that are crucial to HER and OER,[15] respectively, giving it the potential to be a photocatalytic material. Hinnemann studied hydrogen release using MoS_2 nanoparticles supported on graphite as a catalyst for water electrolysis, and he found that the binding free energy of atomic hydrogen to the catalyst was close to zero ($\Delta G^{\circ}_{H} \cong 0.1$ eV).[16] WSe_2 is also considered to be one of the most promising optoelectronic device materials for the future.[17] For example, the photocells based on WSe_2 have high efficiency and thermal stability because of its high charge carrier mobility and mechanical

---

[a] *School of Mechanical Engineering, Shaanxi University of Technology, Hanzhong, Shaanxi, 723001, China. E-mail: hongcui@snut.edu.cn*

[b] *Shaanxi Key Laboratory of Industrial Automation, Shaanxi University of Technology, Hanzhong, Shaanxi, 723001, China*

[c] *School of Physical Science and Technology, Southwest University, Chongqing, 400715, P. R. China*

flexibility.[18–20] Kumar studied the synthesis of heterojunctions using WSe_2 as the substrate and found that $MoSe_2/WSe_2$ showed decent new photoelectric characteristics (enhanced photoluminescence, smaller electron effective masses and high electron mobility).[21] McKone investigated the solar energy conversion efficiency of WSe_2 photocatalytic hydrogen production (67%) using Pt/Ru as a co-catalyst (60%).[22] Meng-Yen Tsai *et al.* found that the Fermi energy levels moved towards VBM and CBM when WSe_2 were P and N doped, respectively,[23] which was favorable for changing the photocatalytic activity of WSe_2.

Photocatalytic heterojunctions based on TMD synthesis have been preliminarily studied. For example, Charlie Tsai *et al.* studied hydrogen release with $MoSe_2/WSe_2$ heterojunctions based on the density function theory (DFT) because $MoSe_2$ and WSe_2 nanofilms and nanosheets have been shown to be active for electrochemical H_2 evolution. They found that enhanced activity was located at the edges of $MoSe_2$ and WSe_2.[24] Wang *et al.* studied the photocatalytic performance of the direct Z-scheme $MoSe_2/SnS_2$ van der Waals heterojunction. They found that the light absorption wavelength was widened to 600 nm, but the oxidation potential could be further increased to produce hydrogen more efficiently.[25] Ho *et al.* deposited MoS_2 on CdS to form a CdS/MoS_2 heterojunction and used it as a photoanode to study its photocatalytic activity. They found that heterojunction formation contributed to increased carrier concentration and conductivity.[26] Hellstern *et al.* studied solar energy conversion efficiency using $MoS_2/TiO_2/CdS/CGSe$ as a photocathode, and they found that the catalyst produced H_2S during the preparation process.[27] Efficiency needs to be improved further to meet the demand for energy.

According to Jiang's study, any MX_2 (M = molybdenum (Mo) and tungsten (W); X = sulphur (S) and selenium (Se)) material cannot be used directly as a full spectrum photocatalyst because its valence band maximum (VBM) and conduction band minimum (CBM) energies do not match the oxidation reduction potential of HER and OER.[28] Monolayer MoS_2 photogenerated electrons and holes have high mobility, which is favorable for photocatalytic hydrogen production.[29–32] In this study, a new design of a photocatalytic van der Waals heterojunction MoS_2/WSe_2 is proposed using TMDs with physical and optoelectronic properties as substrates. In addition, HER and OER generation are studied to enhance the photocatalytic activity with higher redox activity.[23,33]

Methodology

In this paper, we performed the initial calculations using first principles based on DFT and performed the single point calculations with a hybrid functional theory (HSE (06)). We carried out both calculations using the Vienna *ab initio* simulation package (VASP).[34] The exchange correlation function used the Perdew–Burke–Ernzerh (PBE) function of the generalized gradient approximation (GGA). We set the plane wave cutoff energy at 500 eV.[34–39] The effective band structure (EBS) proposed by Zunger *et al.* could transform the band structure of a supercell into the Brillouin region of a primitive cell, which provided favorable conditions for the correct analysis of the supercell energy band. Therefore, we calculated the effective band structure of the supercell by the energy band unfolding method.[40–42] The structure relaxation energy convergence criterion was 1×10^{-6} eV. The force convergence criterion was -2×10^{-2} eV Å^{-2}. The Brillouin region was divided into 6 × 6 × 1 and 4 × 4 × 1 for the hexagonal crystalline MoS_2 and WSe_2 and MoS_2/WSe_2, respectively. The Brillouin regions are shown in Fig. 2(b) and (d), and the calculated path is $\Gamma \rightarrow M \rightarrow K \rightarrow \Gamma$.[43,44] We set the large vacuum space of 20 Å along the perpendicular direction to the 2D plane to minimize the interactions between the adjacent heterostructures. When performing first principles calculations, we introduced HSE (06) to accurately characterize the correct energy band structure and electronic properties of the material. The study used the mixing parameter, $\alpha = 0.25$, for accurate hybrid generalization calculations, because the HSE (06) hybrid generalization results provided more accurate calculations, including those for band structure, density of states (DOS), electronic properties, and work function, compared with PBE functional.[45,46] Therefore, the research in this article is based on the results of HSE (06) hybrid functional calculations.

Results and discussion

TMD exists in several structural phases produced by the coordination of transition metal atoms and different VIA atoms. This study adopted the ABA-stacked trigonal (2H) structure of common structural features. As shown in Fig. 1, the monolayer TMD can be viewed as a sandwich structure consisting of two layers of VIA atoms (A and A′) embedded with one layer of transition metal elements (B and B′).[21,47]

We constructed and optimized the monolayer MoS_2 and monolayer WSe_2 models. The bond lengths of Mo–S and W–Se were 2.412 Å and 2.542 Å, respectively, as shown in Fig. 2(a). Then, we constructed the heterostructure with MoS_2 and WSe_2 model structure particles. After full relaxation as shown in Fig. 2(c), the bond lengths of Mo–S and W–Se were 2.412 Å and 2.542 Å, respectively. As shown in Fig. 2(c), both the semiconductors layer distance was $d = 3.70$ Å, indicating the heterojunction was a van der Waals heterojunction.[48,49] The van der Waals effect enabled the tight bonding of different 2D nanomaterials (MoS_2 and WSe_2), and the van der Waals heterojunctions with ultrafast carrier migration accelerated the charge migration.[50] As shown in Fig. 2(a), the lattice volumes of MoS_2,

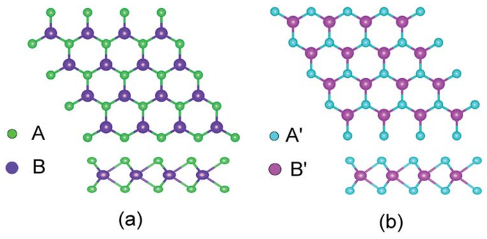

Fig. 1 2(H) MoS_2 (a) and 2(H) WSe_2 (b) structures: green (A) spheres, indigo (B) spheres, cyan (A′) spheres and pink (B′) spheres represent S atoms, Mo atoms, Se atoms and W atoms, respectively.

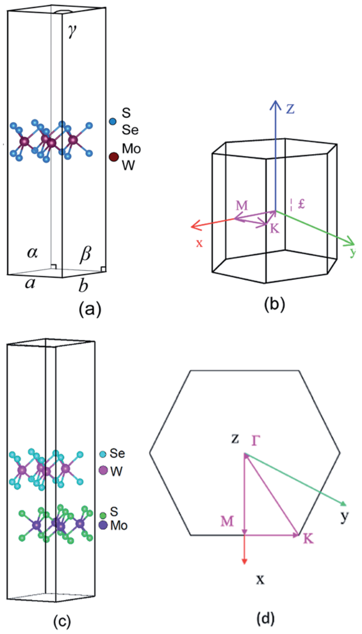

Fig. 2 (a) Spatial structure of the hexagonal crystal MoS_2 and WSe_2: blue and wine spheres represent S, Se atoms and Mo, W atoms; (c) MoS_2/WSe_2 stacked structure of MoS_2 and WSe_2: green, indigo, cyan, and pink spheres represent S atoms, Mo atoms, Se atoms, and W atoms, respectively; (b) Brillion region high symmetry point path schematic three-dimensional view; and (d) top view.

WSe_2, and MoS_2/WSe_2 were 325.63 Å^3, 346.30 Å^3, and 334.22 Å^3, respectively, and E_{MoS_2/WSe_2}, E_{MoS_2}, and E_{WSe_2} were −173.75 eV, −86.987 eV, and −86.485 eV in the constructed MoS_2/WSe_2 heterojunction. The thermodynamic stability of the heterojunction can be achieved with eqn (1):[51]

$$E_b = E_{MoS_2/WSe_2} - E_{WSe_2} - E_{MoS_2} \tag{1}$$

where E_{MoS_2/WSe_2}, E_{WSe_2}, and E_{MoS_2} are the total energy of MoS_2/WSe_2, WSe_2, and MoS_2, respectively.

Here, negative binding energy (−0.287 eV) indicated the MoS_2/WSe_2 heterojunction had stable thermodynamic properties.

The complex process of hydrogen production by photocatalytic WS included the generation, transformation, recombination, and surface reactions of photogenerated electron and hole pairs. We plotted and used the electrostatic potential function diagrams of MoS_2, WSe_2, and MoS_2/WSe_2 heterojunctions to study the photocatalyst carrier transfer and analyze the photocatalytic efficiency, as shown in Fig. 3(a)–(c), respectively. We obtained the work function Φ with eqn (2).[51–54] To further investigate the charge distribution of in the heterojunctions, we plotted the plane average charge density difference in Fig. 3(d) and the charge density difference in Fig. 3(e). The plane average charge density difference and charge density difference $\Delta\rho$ were obtained by eqn (3) and (4), respectively:[55]

$$\Phi = E_{va} - E_f \tag{2}$$

where Φ, E_{va}, and E_f represent work function, vacuum level, and Fermi level, respectively.

$$\Delta\rho_{pavg(z)} = \int_{\sum z} \Delta\rho(r)\mathrm{d}x\mathrm{d}y \tag{3}$$

where $\Delta\rho_{pavg}$ is the plane average charge density difference.

$$\Delta\rho = \rho_{MoS_2/WSe_2} - \rho_{MoS_2} - \rho_{WSe_2} \tag{4}$$

where ρ_{MoS_2/WSe_2}, ρ_{MoS_2}, and ρ_{WSe_2} are the charge density of MoS_2/WSe_2, WSe_2, and MoS_2, respectively.

As shown in Table 1, the work functions of MoS_2, WSe_2, and MoS_2/WSe_2 are 5.25 eV, 4.36 eV, and 4.80 eV, respectively, which is consistent with the PBE functional.[53] The work functions of MoS_2, WSe_2, and MoS_2/WSe_2 are 5.63 eV, 5.08 eV, and 5.22 eV, respectively under the HSE (06) hybrid functional condition. The Fermi energy level of MoS_2 was lower than that of WSe_2, and the electrons flowed spontaneously from WSe_2 to MoS_2 until the Fermi levels on both sides reached the same potential. Thus, the WSe_2 side was positively charged, whereas the MoS_2 side was negatively charged at the interface. Hence, energy band bending would occur and a built-in electric field would be formed at the junction of the MoS_2 surface and WSe_2 surface interface. The formation of a built-in electric field promoted the separation and transport of photogenerated electrons and holes, inhibited the recombination of photogenerated electrons and holes, and prolonged the life of photogenerated electrons and holes, better promoting photogenerated carrier transfers to the HER and OER sites of the MoS_2/WSe_2 heterojunction, and increasing photocatalytic reaction efficiency.

Fig. 3(d) quantitatively depicts the plane averaged charge density difference along the lattice c direction. It is evident that the negative charge accumulated mainly on the MoS_2, whereas positive charge accumulated on the WSe_2. The amount of the charge accumulation and transformation was zero on both sides of the heterojunction, which verified that the thickness of the heterojunction vacuum layer was perfectly suitable to avoid errors in the analytical calculations because of an insufficient vacuum layer thickness. Fig. 3(e) depicts the redistribution of negative charge and positive charge in heterojunctions, with cyan representing the negative charge accumulation region and yellow representing the negative charge depletion region. The negative charge was concentrated mainly on the surface of MoS_2 and around the Mo atoms, and a small amount of negative charge aggregation appeared inside WSe_2 between W and Se atoms. Electron depletion occurred on the WSe_2 semiconductor. The MoS_2 semiconductor had a small amount of charge migration between the Mo and S atoms. Fig. 3(d) and (e) showed the redistribution of negative and positive charge on different semiconductors resulting from the built-in electric field directed from the WSe_2 surface toward the MoS_2 surface. The redistribution of charge was in agreement with the formation of a built-in electric field and the work function, which favored the photocatalytic reaction.[56]

Under illumination, the electrons on photocatalyst VB absorbed photon energy and then became excited from the VB to CB, and the photogenerated holes remained on the VB. For

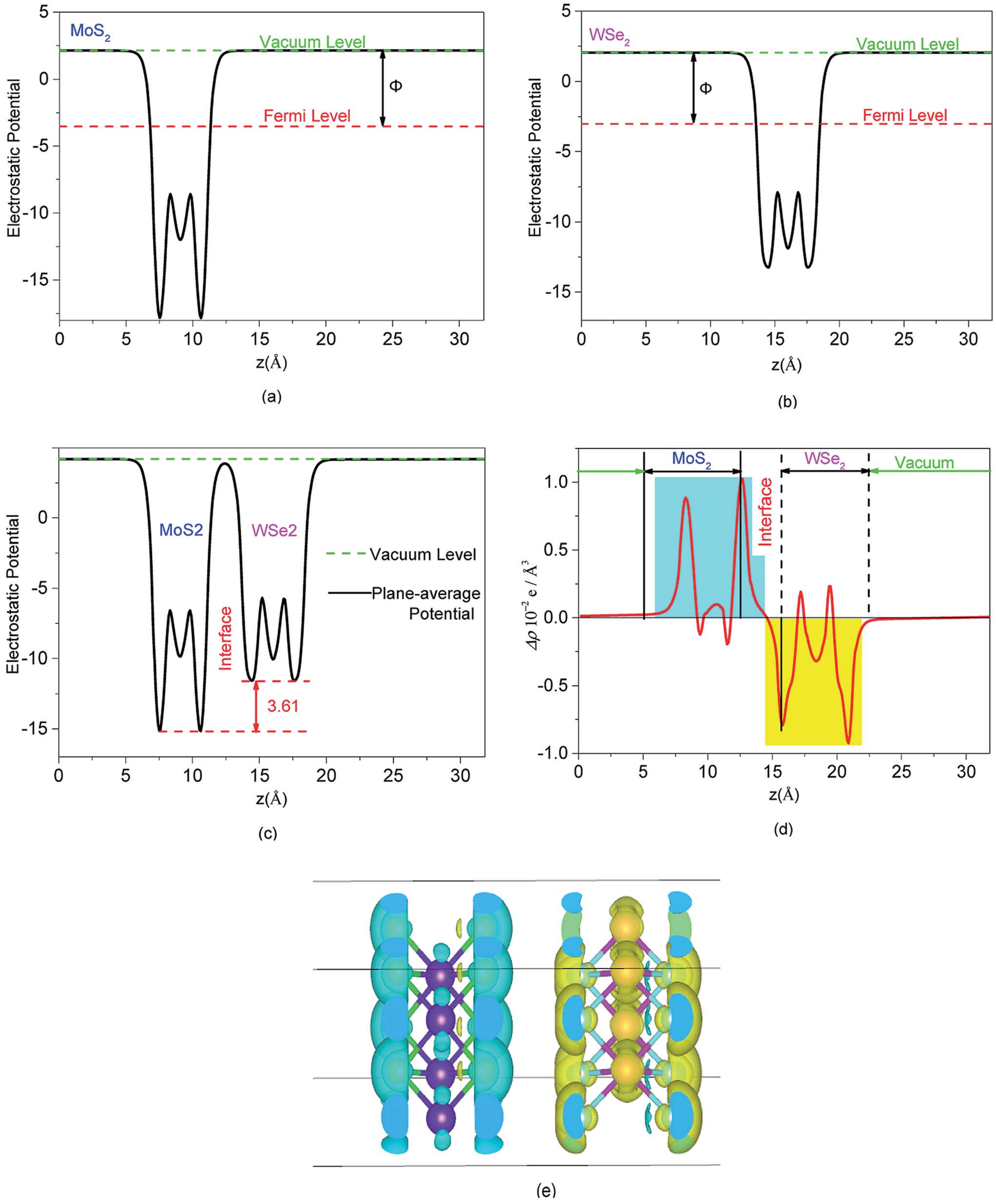

Fig. 3 Electrostatic potential of (a) MoS_2, (b) WSe_2, and (c) MoS_2/WSe_2; (d) plane average charge density difference; and (e) the charge density difference for MoS_2/WSe_2, where cyan and yellow represent charge accumulation and depletion, respectively.

direct bandgap semiconductors, the electrons on the VB with energy greater than or equal to the bandgap jumped directly from the VB to the CB at the bandgap.[57] To study the photocatalytic properties of the photocatalyst, we first calculated the energy bands of MoS_2 and WSe_2 by the PBE function to prepare the HSE (06) hybrid function calculations. The CBM

Table 1 Vacuum energy level, Fermi energy level and work function corresponding to MoS_2, WSe_2, and the MoS_2/WSe_2 heterojunction

	E_{va} (eV)		E_f (eV)		Φ	
Materials	PBE	HSE (06)	PBE	HSE (06)	PBE	HSE (06)
MoS_2	2.36	2.13	−2.89	−3.50	5.25	5.63
WSe_2	4.26	2.05	−0.1	−3.03	4.36	5.08
MoS_2/WSe_2	4.19	4.20	−0.61	−0.83	4.80	5.22

and the VBM were displayed at the *K* point in the Brillouin region. The results, under the PBE functional, showed that the bandgap (1.68 eV) of the monolayer MoS_2 was consistent with Manzeli's experimental results (1.71 eV), and the bandgap (1.60 eV) of the monolayer WSe_2 was consistent with Lee's experimental results (1.66 eV).[47,58,59] The energy band structures of MoS_2, WSe_2, and MoS_2/WSe_2 were further calculated by HSE (06) hybrid function. Thus, a more precise analysis of the efficiency of heterojunction photocatalytic hydrogen production is shown in Fig. 4. In Fig. 4(a), the CBM and VBM of monolayer MoS_2 lie in the *K* point in the Brillouin region. So, the monolayer MoS_2 was a direct bandgap, which was consistent with the conclusion that the direct bandgap E_g was 2.16 eV, and the previous calculations were in agreement with the experimental results of Manzeli (2.16 eV) and Hill (2.16 ± 0.04 eV).[47,60] Fig. 4(b) shows the energy band structure of the monolayer WSe_2, with both its CBM and VBM appearing at the *K* point (direct bandgap 2.08 eV), which was consistent with the experimental results of Zribi (2.08 eV), and Chiu (2.08 ± 0.1 eV).[61,62] This result demonstrated that the calculation method was correct. Fig. 4(c) shows both the heterojunction CBM and VBM obtained at the *K* point, which can broaden the light absorption range. In addition, the CBM and VBM of MoS_2 were contributed to primarily by Mo atoms. The CBM and VBM of WSe_2 were contributed to primarily by W atoms with a small contribution from Se atoms, whereas the VB was contributed to primarily by Se atoms. The MoS_2/WSe_2 heterojunction CBM was contributed to primarily by the Mo atoms, and the VBM was contributed to primarily by W atoms.

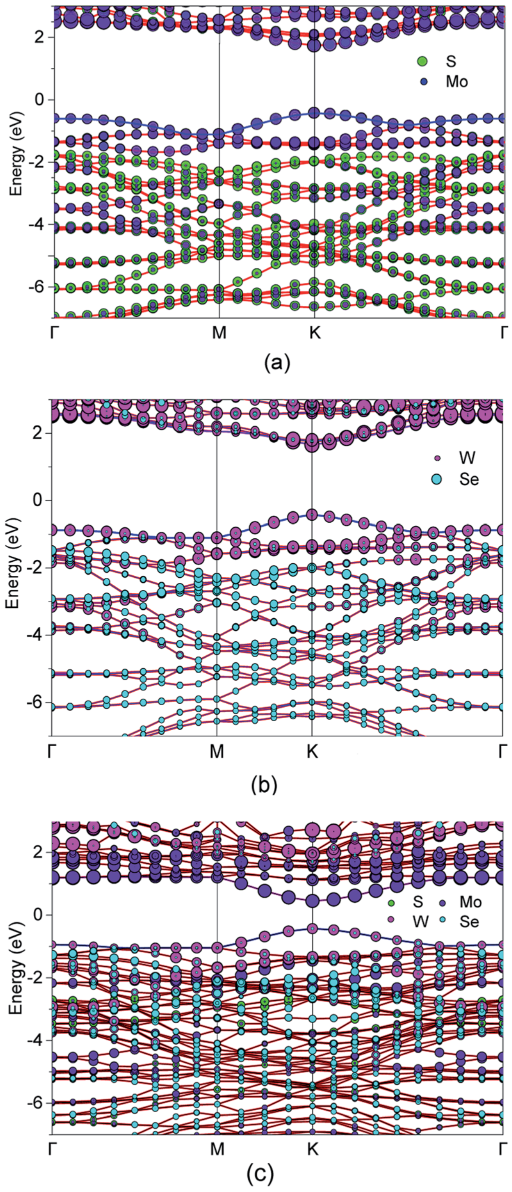

Fig. 4 Energy band structure of (a) MoS_2, (b) WSe_2, and (c) the MoS_2/WSe_2 heterojunction.

To quantitatively investigate the interface electronic structure and identification of the nature of the orbitals, we calculated the projected density of state (PDOS) of the MoS_2, WSe_2, and the MoS_2/WSe_2 heterostructure, and the total density of state (TDOS) of the MoS_2/WSe_2 heterostructure in Fig. 5. Fig. 5(a) indicates that the VBM and CBM of the MoS_2 were occupied by the Mo(d) atomic orbitals of MoS_2. Fig. 5(b) indicates that the VBM and CBM of the WSe_2 were occupied by the W(d) atomic orbitals of WSe_2. Fig. 5(c) indicates that the VBM of the MoS_2/WSe_2 heterostructure was occupied by the atomic orbitals of WSe_2. The CBM of the MoS_2/WSe_2 heterostructure was occupied primarily by the atomic orbitals of MoS_2, and the atomic orbitals of MoS_2 were higher than those of WSe_2. Fig. 5(d)–(f) show that the VBM and CBM of the MoS_2/WSe_2 heterostructure were occupied by the W atoms and Mo atoms, respectively. Fig. 5(e) and (f) further show that the W(s) and W(p) orbital contributions of WSe_2 were smaller than those of W(d) orbits, and the Mo(s) and Mo(p) orbital contributions of MoS_2, which were significantly smaller than those of the Mo(d) orbits. Most importantly, this analysis of DOS was in agreement with the results of the band structure, as shown in Fig. 4(a)–(c).

Combining the analysis of the work function and the Fermi level in Fig. 3, we studied the mechanism of hydrogen production by photocatalytic WS of MoS_2/WSe_2. As shown on the left side of Fig. 6(a), the Fermi level of MoS_2 was lower than that of WSe_2. An electrostatic potential difference formed because of the difference between Fermi levels when MoS_2 and WSe_2 were in contact, and the electrons flowed spontaneously from the high Fermi level to the low Fermi level under the drive of the potential difference until the Fermi levels reach equilibrium. Hence, the positive charge and negative charge accumulated mainly on the WSe_2 side and MoS_2 sides at the interface,

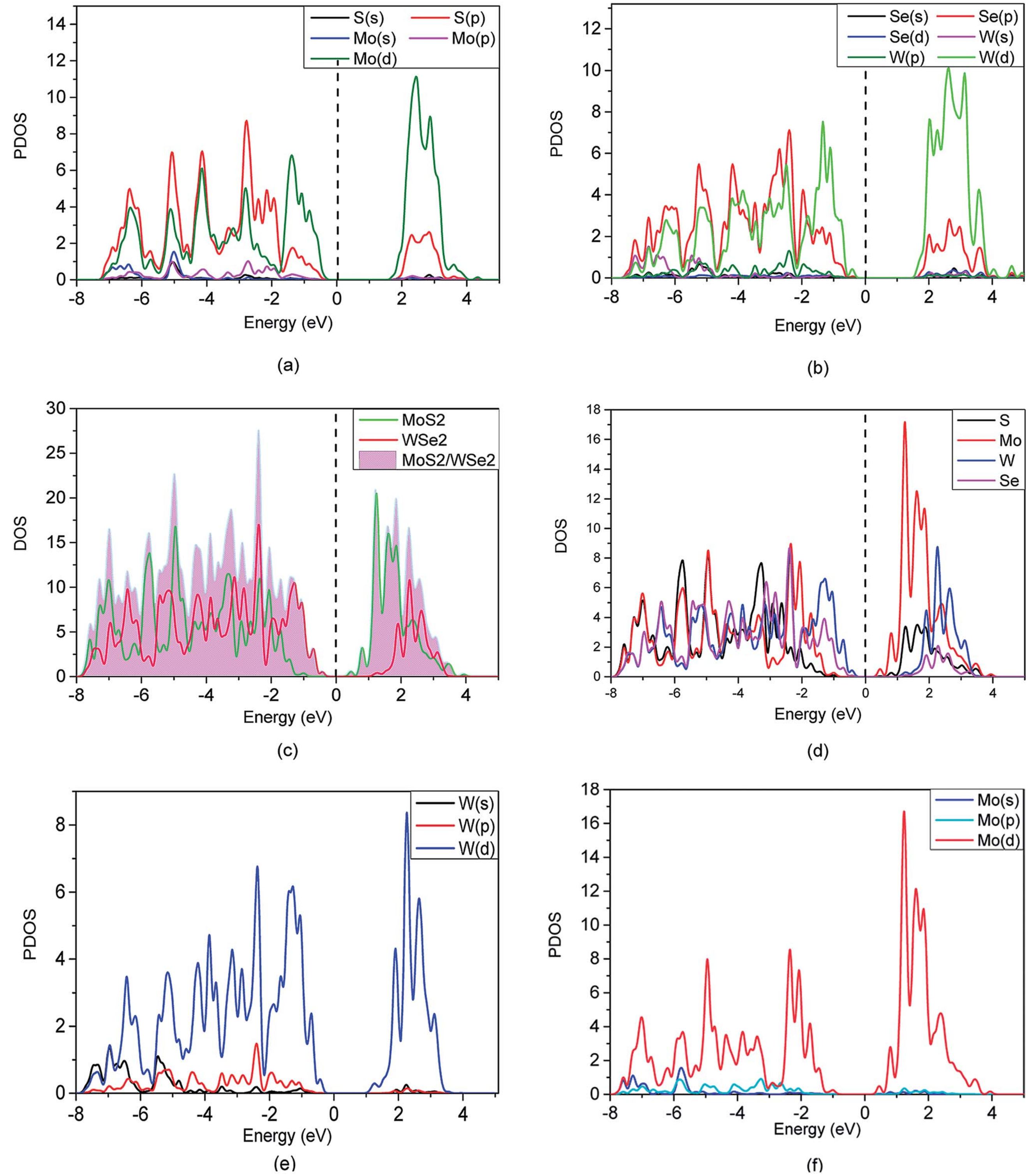

Fig. 5 PDOS of (a) MoS_2, (b) WSe_2, and (c) TDOS and PDOS of the MoS_2/WSe_2 heterostructure; (d) PDOS of the heterostructure; (e) PDOS of the W elements on the VB of heterostructure; and (f) PDOS of the Mo elements on the CB of heterostructure.

respectively. Then a built-in electric field from WSe_2 to MoS_2 formed at the junction of the MoS_2 surface and WSe_2 surface interface, and the VB of WSe_2 and CB of MoS_2 occurred by bending upward and downward, respectively, as shown in Fig. 6(a) (right). The photocatalytic reaction mechanism and transfer of photogenerated electrons and holes of the MoS_2/WSe_2 heterostructure are illustrated in Fig. 6(b). Under illumination, electrons absorbed photon energy and then became excited from the VB of MoS_2 and WSe_2 to their CB; simultaneously, photoexcited holes were left in their VB. The built-in

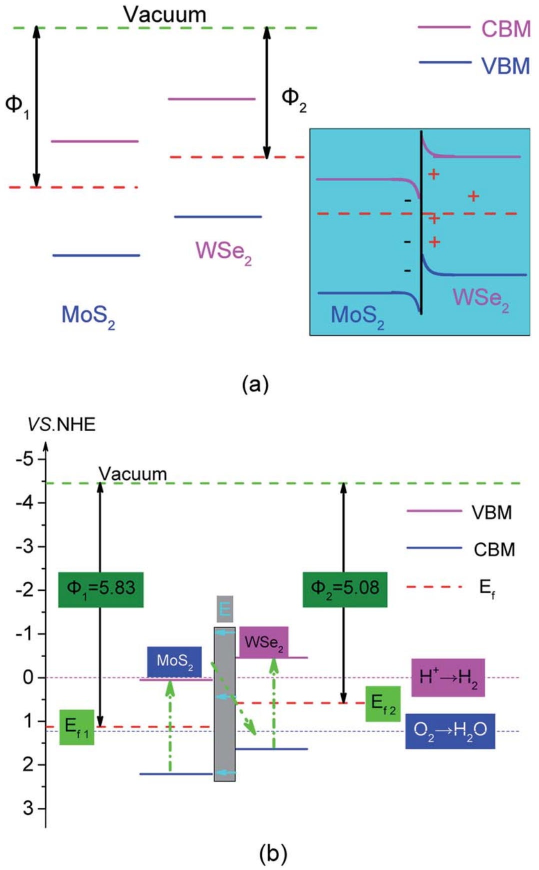

Fig. 6 (a) Z-scheme semiconductor staggered energy band principles, untouched (left), touched (right); and (b) MoS_2 and WSe_2 band alignment. The pink solid line in the figure corresponds to the CBM in Fig. 4(a) and (b), the blue solid line corresponds to the VBM in Fig. 4(a) and (b); the red dotted line, green dotted line, pink dotted line, and blue dotted line represent the Fermi level, the vacuum level, the minimum reduction potential of hydrogen generated by WS, and the minimum oxidation potential of the water oxidation reaction, respectively.

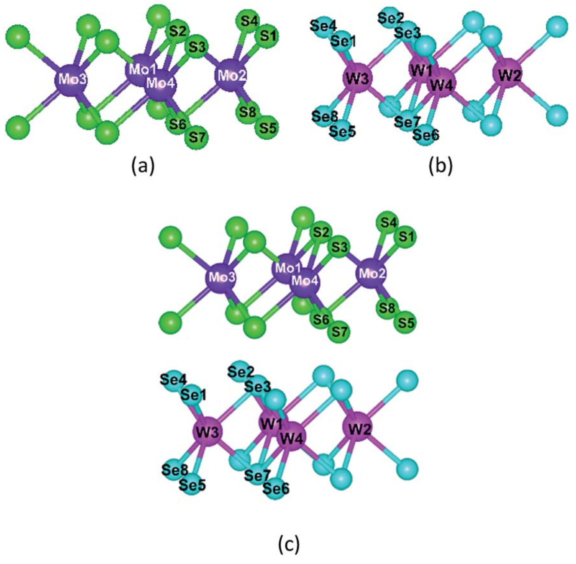

Fig. 7 Atomic number of semiconductor materials: (a) MoS_2, (b) WSe_2, and (c) MoS_2/WSe_2 heterostructure.

Table 2 The amount of atomic charge before the semiconductor material (MoS_2 and WSe_2) forms a heterojunction

Elements	Charge (*e*)	Elements	Charge (*e*)
S1	−0.95046	W1	0.96352
S2	−0.95027	W2	0.96713
S3	−0.95041	W3	0.96713
S4	−0.95024	W4	0.97074
S5	−0.93441	Se1	−0.45907
S6	−0.93408	Se2	−0.45907
S7	−0.93441	Se3	−0.45907
S8	−0.93401	Se4	−0.45907
Mo1	1.88457	Se5	−0.50806
Mo2	1.88457	Se6	−0.50806
Mo3	1.88457	Se7	−0.50806
Mo4	1.88457	Se8	−0.50806

electric field from WSe_2 surface to MoS_2 surface accelerated the transfer of photoexcited electrons from the CB of MoS_2 to the VB of WSe_2, and resulted in the recombination of electrons and holes in the VB of WSe_2. Simultaneously, the built-in electric field also restrained the photoexcited electrons in the CB of WSe_2 to flow into the CB of MoS_2 and photoexcited holes in the VB of MoS_2 to transfer to the VB of WSe_2. Therefore, under the built-in electric field driving, photoexcited electrons in the CB of MoS_2 and holes in the VB of WSe_2 were consumed. Conversely, the photoexcited electrons and holes naturally accumulated in the CB of WSe_2 and VB of MoS_2, respectively. The separation of photoexcited electrons and holes in space prolonged their lifetime and increased the probability of the photoexcited electrons and holes participating in the HER and OER on the surface, respectively, which effectively improved the photocatalytic activity of the MoS_2/WSe_2 heterostructure. This analysis indicated that MoS_2/WSe_2 heterostructure was a direct Z-scheme photocatalyst.[2,63] As shown in Fig. 6(b), the photoexcited electrons of direct Z-scheme MoS_2/WSe_2 heterostructure accumulated in the CB of WSe_2, and the CB edge potential of WSe_2 was −0.421 eV (*vs.* NHE), which was more negative than that of H^+/H_2 (0 eV), and had enough ability to reduce H^+ to H_2. Additionally, the photoexcited holes accumulated at the VB of MoS_2,

Table 3 The amount of atomic charge MoS_2/WSe_2 heterojunction

Elements	Charge (*e*)	Elements	Charge (*e*)
S1	−0.58967	W1	0.92161
S2	−0.58968	W2	0.92161
S3	−0.58953	W3	0.92163
S4	−0.58969	W4	0.92138
S5	−0.58667	Se1	−0.4471
S6	−0.58668	Se2	−0.44709
S7	−0.58668	Se3	−0.44712
S8	−0.58669	Se4	−0.44712
Mo1	1.17307	Se5	−0.47121
Mo2	1.17307	Se6	−0.47121
Mo3	1.17306	Se7	−0.47098
Mo4	1.17293	Se8	−0.47124

and the corresponding VB edge potential of MoS_2 was 2.256 eV, which was more positive than that of O_2/H_2O (1.23 eV) and had sufficient ability to produce O_2. Therefore, the direct Z-scheme MoS_2/WSe_2 heterostructure exhibited better photocatalytic performance than either MoS_2 or WSe_2 alone.

The charge transfer of the photocatalyst determined the hydrogen production efficiency of the photocatalyst, and we calculated the Bader charge to study the charge transformation in the catalyst.[64,65]

As shown in Fig. 7, we calculated the Bader charge of MoS_2, WSe_2, and MoS_2/WSe_2 heterostructure and plotted Tables 2 and 3 based on the number of charges carried by each atom. Mo and S atoms are more charged than W and Se atoms, respectively. Transition metal atoms are twice as charged as S-group atoms.

Table 4 Energy of different adsorption sites. E_{H_2}, E_h, and E_{h-H_2} represent the energy of hydrogen molecules, heterojunction, and the heterojunction after hydrogen adsorption, respectively. In addition, E_F represents the free energy of H adsorption at various sites of the heterostructures. The E_F can be achieved with eqn (5):[66]

Sites	E_{H_2} (eV)	E_{h-H_2} (eV)	E_F (eV)
Se1	−6.77	−180.32	0.26
Se2	−6.76	−180.32	0.25
Se3	−6.76	−180.32	0.25
Se4	−6.76	−180.32	0.25

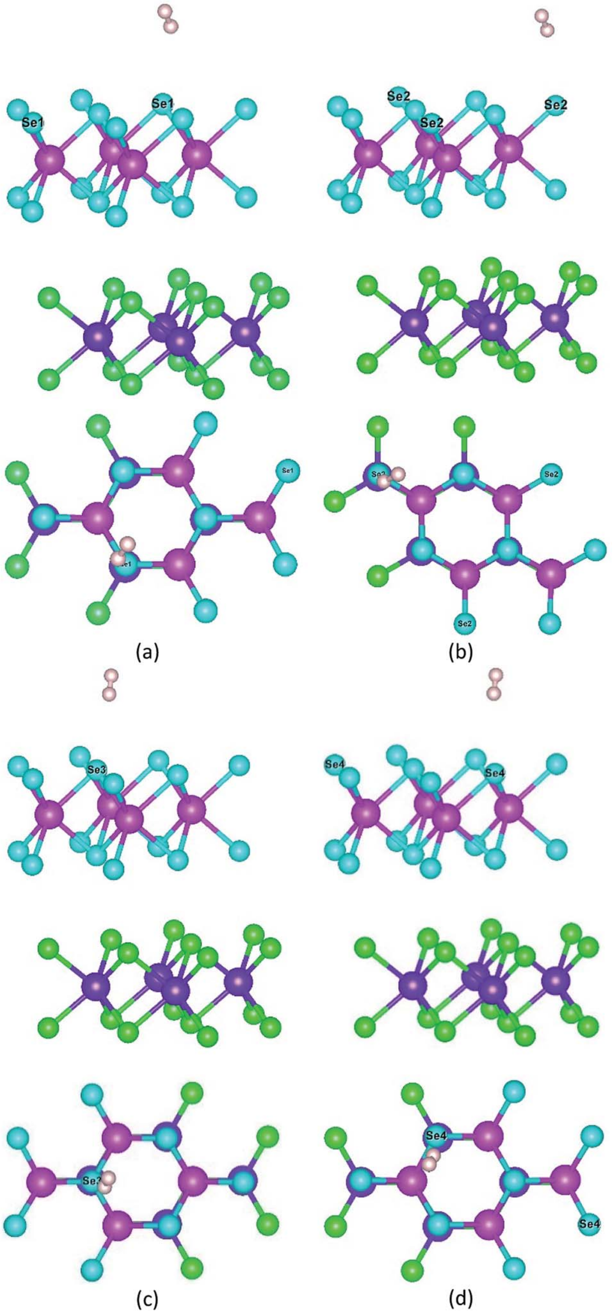

Fig. 8 Hydrogen adsorption model for different adsorption sites: (a) Se1 site, (b) Se2 site, (c) Se3 site, and (d) Se4 site.

Combining Tables 2 and 3, it is found that the charge of all elements in the heterojunction decreases when MoS_2 forms a heterojunction with WSe_2, especially the charge of Mo, S atoms decreases more than that of W, Se atoms, which indicates that part of the electrons of MoS_2 move to WSe_2, which is consistent with the results of the previous analysis, and indicates that the charge of MoS_2 and WSe_2 is partially free in the heterojunction as free electrons and does not participate in atomic bonding, which helps to improve the hydrogen production efficiency of the photocatalyst.

As shown in Fig. 8, to characterize the efficiency of photocatalytic WS for hydrogen production, we constructed a hydrogen adsorption model for the heterojunction and calculated the adsorption free energy for hydrogen at the different sites. The adsorption free energy data are shown in Table 4.

$$E_F = E_{h-H_2} - E_h - E_{H_2} + 0.24 \tag{5}$$

As shown in Table 4, the free energies of Se1, Se2, Se3, and Se4 atoms for hydrogen were 0.26 eV, 0.25 eV, 0.25 eV, and 0.25 eV, respectively. They all were close to 0 eV, which indicated that the heterojunction did not have the adsorption effect on hydrogen after the generation of hydrogen, and the generated hydrogen could actively diffuse and failed to form hydrogen molecules clustered around the active site.[67]

Conclusions

In this study, we designed a MoS_2/WSe_2 van der Waals heterojunction to improve the efficiency of photocatalytic WS for hydrogen evolution. We performed all computations, including structure relaxation, energy band, DOS, electronic properties, and work function, based on DFT and HSE (06). Before performing the HSE (06) calculations, we used DFT based on the first principles for the initial calculations. We analyzed all results based on calculations of HSE (06) hybrid functional theory. The energy calculation results showed that the formation energy of the MoS_2/WSe_2 heterojunction was negative, so the thermodynamic properties of the heterojunction were stable. The work function calculations showed that the electrons flowed spontaneously from WSe_2 to MoS_2 until a potential equilibrium was reached on both semiconductors after the formation of the heterojunction, which resulted in an accumulation of a charge on one side of the heterojunction. Hence, a built-in electric field was established within the heterojunction that prevented the flow of photogenerated electrons from the CB of WSe_2 to that of MoS_2, stopped the flow of holes from the VB of MoS_2 to WSe_2, and facilitated the flow of photogenerated electrons from the MoS_2 CB to recombine with the holes in the VB of WSe_2. In this way, photogenerated electrons and holes accumulated in the CB of WSe_2 and the VB of MoS_2, respectively. This meant that reduction reactions proceeded at WSe_2 and oxidation reactions proceeded at MoS_2. The energy band calculations showed that the monolayer MoS_2 and WSe_2 both had direct bandgaps. When MoS_2 and WSe_2 were in contact, the CB potential of WSe_2 was more negative than that of MoS_2, and the VB potential of MoS_2 was more positive than the VBM of WSe_2. The orbital contributions of each element in MoS_2, WSe_2, and MoS_2/WSe_2 to VBM and CBM in combination with the DOS-assisted energy band structures were also analyzed. All of the results indicated that MoS_2/WSe_2 was a direct Z-scheme heterojunction. Photocatalytic HER and OER occurred on the CB of WSe_2 and the VB of MoS_2. Finally, we calculated the Bader charges of MoS_2, WSe_2, and MoS_2/WSe_2 and analyzed the charge transfer characterization active sites. We constructed the heterojunction hydrogen adsorption model to analyze the adsorption performance of heterojunction on hydrogen after hydrogen generation. All of the results showed that MoS_2/WSe_2, with great thermodynamic stability and strong redox ability, could be used as a WS catalyst for hydrogen production.

Conflicts of interest

There are no conflicts to declare.

Acknowledgements

This research was funded by the National Natural Science Foundation of China (No. 61701288, No. 51706128), the Key Scientific Research Project of the Shaanxi Provincial Education Department (No. 20JS019) and the Postgraduate Innovation Project of the Shaanxi University of Technology (No. SLGYCX2026).

References

1 L. Yang, X. Li, G. Zhang, P. Cui, X. Wang, X. Jiang, J. Zhao, Y. Luo and J. Jiang, *Nat. Commun.*, 2017, **8**, 16049.
2 Q. Xu, L. Zhang, J. Yu, S. Wageh, A. A. Al-Ghamdi and M. Jaroniec, *Mater. Today*, 2018, **21**, 1042–1063.
3 M. Z. Rahman, M. G. Kibria and C. B. Mullins, *Chem. Soc. Rev.*, 2020, **49**, 1887–1931.
4 A. Fujishima and K. Honda, *Nature*, 1972, **238**, 37–38.
5 C. A. Rodriguez, M. A. Modestino, D. Psaltis and C. Moser, *Energy Environ. Sci.*, 2014, **7**, 3828–3835.
6 H. Sun, C. Tian, G. Fan, J. Qi, Z. Liu, Z. Yan, F. Cheng, J. Chen, C.-P. Li and M. Du, *Adv. Funct. Mater.*, 2020, 1910596.
7 Y.-J. Yuan, D. Chen, Z.-T. Yu and Z.-G. Zou, *J. Mater. Chem. A*, 2018, **6**, 11606–11630.
8 J. Yan, T. Wang, G. Wu, W. Dai, N. Guan, L. Li and J. Gong, *Adv. Mater.*, 2015, **27**, 1580–1586.
9 A. K. Geim and K. S. Novoselov, *Nat. Mater.*, 2007, **6**, 183–191.
10 R. Tenne, L. Margulis, M. Genut and G. Hodes, *Nature*, 1992, **360**, 444–446.
11 X. Yu and K. Sivula, *Chem. Mater.*, 2017, **29**, 6863–6875.
12 D. Braga, I. Gutiérrez Lezama, H. Berger and A. F. Morpurgo, *Nano Lett.*, 2012, **12**, 5218–5223.
13 D. Voiry, J. Yang and M. Chhowalla, *Adv. Mater.*, 2016, **28**, 6197–6206.
14 D.-H. Kang, S. R. Pae, J. Shim, G. Yoo, J. Jeon, J. W. Leem, J. S. Yu, S. Lee, B. Shin and J.-H. Park, *Adv. Mater.*, 2016, **28**, 7799–7806.
15 O. Lopez-Sanchez, D. Lembke, M. Kayci, A. Radenovic and A. Kis, *Nat. Nanotechnol.*, 2013, **8**, 497–501.
16 B. Hinnemann, P. G. Moses, J. Bonde, K. P. Jørgensen, J. H. Nielsen, S. Horch, I. Chorkendorff and J. K. Nørskov, *J. Am. Chem. Soc.*, 2005, **127**, 5308–5309.
17 S. Das, R. Gulotty, A. V. Sumant and A. Roelofs, *Nano Lett.*, 2014, **14**, 2861–2866.
18 G. Prasad and O. N. Srivastava, *J. Phys. D: Appl. Phys.*, 1988, **21**, 1028–1030.
19 H.-Y. Park, S. R. Dugasani, D.-H. Kang, J. Jeon, S. K. Jang, S. Lee, Y. Roh, S. H. Park and J.-H. Park, *ACS Nano*, 2014, **8**, 11603–11613.
20 N. T. Nguyen, P. A. Berseth, Q. Lin, C. Chiritescu, D. G. Cahill, A. Mavrokefalos, L. Shi, P. Zschack, M. D. Anderson, I. M. Anderson and D. C. Johnson, *Chem. Mater.*, 2010, **22**, 2750–2756.
21 S. Kumar and U. Schwingenschlögl, *Chem. Mater.*, 2015, **27**, 1278–1284.
22 J. R. McKone, A. P. Pieterick, H. B. Gray and N. S. Lewis, *J. Am. Chem. Soc.*, 2013, **135**, 223–231.
23 M.-Y. Tsai, S. Zhang, P. M. Campbell, R. R. Dasari, X. Ba, A. Tarasov, S. Graham, S. Barlow, S. R. Marder and E. M. Vogel, *Chem. Mater.*, 2017, **29**, 7296–7304.
24 C. Tsai, K. Chan, F. Abild-Pedersen and J. K. Nørskov, *Phys. Chem. Chem. Phys.*, 2014, **16**, 13156–13164.
25 B. Wang, X. Wang, H. Yuan, T. Zhou, J. Chang and H. Chen, *Int. J. Hydrogen Energy*, 2020, **45**, 2785–2793.
26 T. A. Ho, C. Bae, J. Joe, H. Yang, S. Kim, J. H. Park and H. Shin, *ACS Appl. Mater. Interfaces*, 2019, **11**, 37586–37594.
27 T. R. Hellstern, D. W. Palm, J. Carter, A. D. DeAngelis, K. Horsley, L. Weinhardt, W. Yang, M. Blum, N. Gaillard, C. Heske and T. F. Jaramillo, *ACS Appl. Energy Mater.*, 2019, **2**, 1060–1066.
28 H. Jiang, *J. Phys. Chem. C*, 2012, **116**, 7664–7671.
29 Y. Zhang, J. Ye, Y. Matsuhashi and Y. Iwasa, *Nano Lett.*, 2012, **12**, 1136–1140.
30 G. L. Chiarello, M. H. Aguirre and E. Selli, *J. Catal.*, 2010, **273**, 182–190.

31 Q. Xiang, J. Yu and M. Jaroniec, *J. Am. Chem. Soc.*, 2012, **134**, 6575–6578.

32 C. Hu, X. Wang and B. Song, *Light: Sci. Appl.*, 2020, **9**, 88.

33 L. Li, R. Long and O. V. Prezhdo, *Chem. Mater.*, 2017, **29**, 2466–2473.

34 G. Kresse and J. Furthmüller, *Phys. Rev. B: Condens. Matter Mater. Phys.*, 1996, **54**, 11169–11186.

35 P. E. Blöchl, *Phys. Rev. B: Condens. Matter Mater. Phys.*, 1994, **50**, 17953–17979.

36 G. Kresse and D. Joubert, *Phys. Rev. B: Condens. Matter Mater. Phys.*, 1999, **59**, 1758–1775.

37 G. Kresse and J. Furthmüller, *Comput. Mater. Sci.*, 1996, **6**, 15–50.

38 K. Dolui, I. Rungger, C. Das Pemmaraju and S. Sanvito, *Phys. Rev. B: Condens. Matter Mater. Phys.*, 2013, **88**, 075420.

39 K. E. Aretouli, D. Tsoutsou, P. Tsipas, J. Marquez-Velasco, S. Aminalragia Giamini, N. Kelaidis, V. Psycharis and A. Dimoulas, *ACS Appl. Mater. Interfaces*, 2016, **8**, 23222–23229.

40 Y. Tan, F. W. Chen and A. W. Ghosh, *Appl. Phys. Lett.*, 2016, **109**, 101601.

41 V. Popescu and A. Zunger, *Phys. Rev. Lett.*, 2010, **104**, 236403.

42 V. Popescu and A. Zunger, *Phys. Rev. B: Condens. Matter Mater. Phys.*, 2012, **85**, 085201.

43 Z. Wang, Q. Chen and J. Wang, *J. Phys. Chem. C*, 2015, **119**, 4752–4758.

44 Y. Hinuma, G. Pizzi, Y. Kumagai, F. Oba and I. Tanaka, *Comput. Mater. Sci.*, 2017, **128**, 140–184.

45 J. E. Peralta, J. Heyd, G. E. Scuseria and R. L. Martin, *Phys. Rev. B: Condens. Matter Mater. Phys.*, 2006, **74**, 073101.

46 J. Heyd, G. E. Scuseria and M. Ernzerhof, *J. Chem. Phys.*, 2003, **118**, 8207–8215.

47 S. Manzeli, D. Ovchinnikov, D. Pasquier, O. V. Yazyev and A. Kis, *Nat. Rev. Mater.*, 2017, **2**, 17033.

48 D. S. C. Black, D. C. Craig and D. B. McConnell, *J. Am. Chem. Soc.*, 1996, **118**, 8148–8149.

49 A. Bondi, *J. Phys. Chem.*, 1964, **68**, 441–451.

50 J. Zhang, H. Hong, C. Lian, W. Ma, X. Xu, X. Zhou, H. Fu, K. Liu and S. Meng, *Adv. Sci.*, 2017, **4**, 1700086.

51 L. Huang, N. Huo, Y. Li, H. Chen, J. Yang, Z. Wei, J. Li and S.-S. Li, *J. Phys. Chem. Lett.*, 2015, **6**, 2483–2488.

52 A. Zangwill and D. D. Vvedensky, *Nano Lett.*, 2011, **11**, 2092–2095.

53 Q. Peng, Z. Wang, B. Sa, B. Wu and Z. Sun, *Sci. Rep.*, 2016, **6**, 31994.

54 R. Garg, N. K. Dutta and N. R. Choudhury, *Nanomaterials*, 2014, **4**, 267–300.

55 Y. Yuan, X. Gong and H. Wang, *Phys. Chem. Chem. Phys.*, 2015, **17**, 11375–11381.

56 F. Wang, P. He, Y. Li, T. A. Shifa, Y. Deng, K. Liu, Q. Wang, F. Wang, Y. Wen, Z. Wang, X. Zhan, L. Sun and J. He, *Adv. Funct. Mater.*, 2017, **27**, 1605802.

57 A. Splendiani, L. Sun, Y. Zhang, T. Li, J. Kim, C.-Y. Chim, G. Galli and F. Wang, *Nano Lett.*, 2010, **10**, 1271–1275.

58 Z. Sun, A. Martinez and F. Wang, *Nat. Photonics*, 2016, **10**, 227–238.

59 C.-H. Lee, G.-H. Lee, A. M. van der Zande, W. Chen, Y. Li, M. Han, X. Cui, G. Arefe, C. Nuckolls, T. F. Heinz, J. Guo, J. Hone and P. Kim, *Nat. Nanotechnol.*, 2014, **9**, 676–681.

60 H. M. Hill, A. F. Rigosi, K. T. Rim, G. W. Flynn and T. F. Heinz, *Nano Lett.*, 2016, **16**, 4831–4837.

61 J. Zribi, L. Khalil, B. Zheng, J. Avila, D. Pierucci, T. Brulé, J. Chaste, E. Lhuillier, M. C. Asensio, A. Pan and A. Ouerghi, *npj 2D Mater. Appl.*, 2019, **3**, 27.

62 M.-H. Chiu, C. Zhang, H.-W. Shiu, C.-P. Chuu, C.-H. Chen, C.-Y. S. Chang, C.-H. Chen, M.-Y. Chou, C.-K. Shih and L.-J. Li, *Nat. Commun.*, 2015, **6**, 7666.

63 Y. Li, Y.-K. Peng, L. Hu, J. Zheng, D. Prabhakaran, S. Wu, T. J. Puchtler, M. Li, K.-Y. Wong, R. A. Taylor and S. C. E. Tsang, *Nat. Commun.*, 2019, **10**, 4421.

64 F. Ma, Y. Jiao, G. Gao, Y. Gu, A. Bilic, Z. Chen and A. Du, *Nano Lett.*, 2016, **16**, 3022–3028.

65 G. Henkelman, A. Arnaldsson and H. Jónsson, *Comput. Mater. Sci.*, 2006, **36**, 354–360.

66 L.-X. Dai, X.-Y. Wang, S.-S. Yang, T. Zhang, P.-J. Ren, J.-Y. Ye, B. Nan, X.-D. Wen, Z.-Y. Zhou, R. Si, C.-H. Yan and Y.-W. Zhang, *J. Mater. Chem. A*, 2018, **6**, 11270–11280.

67 M. Cheng, H. Geng, Y. Yang, Y. Zhang and C. C. Li, *Chem.–Eur. J.*, 2019, **25**, 8579–8584.